

Nanoscale

Accepted Manuscript



This is an *Accepted Manuscript*, which has been through the Royal Society of Chemistry peer review process and has been accepted for publication.

Accepted Manuscripts are published online shortly after acceptance, before technical editing, formatting and proof reading. Using this free service, authors can make their results available to the community, in citable form, before we publish the edited article. We will replace this *Accepted Manuscript* with the edited and formatted *Advance Article* as soon as it is available.

You can find more information about *Accepted Manuscripts* in the [Information for Authors](#).

Please note that technical editing may introduce minor changes to the text and/or graphics, which may alter content. The journal's standard [Terms & Conditions](#) and the [Ethical guidelines](#) still apply. In no event shall the Royal Society of Chemistry be held responsible for any errors or omissions in this *Accepted Manuscript* or any consequences arising from the use of any information it contains.

ARTICLE

Ag/g-C₃N₄ catalyst with superior catalytic performance for the degradation of dyes: a borohydride-generated superoxide radicals approach

Cite this: DOI: 10.1039/x0xx00000x

Yongsheng Fu^{1,†}, Tinghuang^{1,†}, Lili Zhang^{2,*}, Junwu Zhu^{1,*} and Xin Wang^{1,*}Received 00th January 2012,
Accepted 00th January 2012

DOI: 10.1039/x0xx00000x

www.rsc.org/

A straightforward approach is developed for fabrication of a visible-light-driven Ag/g-C₃N₄ catalyst. Morphology observation shows that the g-C₃N₄ sheets are decorated with highly dispersed Ag nanoparticles having an average size of 5.6 nm. The photocatalytic activity measurements demonstrate that the photocatalytic degradation rates of methyl orange (MO), methylene blue (MB), and neutral dark yellow GL (NDY-GL) over Ag/g-C₃N₄-4 can reach up to 98.2, 99.3 and 99.6% in the presence of borohydride ions (BH₄⁻) only for 8, 45, and 16 min visible light irradiation, respectively. The significant enhancement in photoactivity of the catalyst is mainly attributed to the high dispersity and smaller size of Ag nanoparticles, the strong surface plasmon resonance (SPR) effect of metallic Ag nanoparticles, the efficient separation of photogenerated charge carriers, the additional superoxide radicals (O₂⁻) generated from the reduction of dissolved oxygen in the presence of BH₄⁻ and the synergistic effect of Ag nanoparticles and g-C₃N₄.

Introduction

As the largest available carbon-neutral energy source, solar energy can not only offer huge energy resources, but also save large amounts of fossil fuels and therefore protect environment. Semiconductor-based photocatalysis has attracted increasing attention as a potential environmental technology for removing pollutants under sunlight irradiation.¹⁻⁴ It has been recognized that the UV region occupies only around 4% of the entire solar spectrum, while the visible light accounts for 45% of the total energy. Accordingly, visible light utilization through semiconductor-based photocatalysis is crucial for solar chemical conversion processes and many visible-light-driven photocatalysts have been successfully developed.⁵⁻⁸

Recently, graphene-based visible light photocatalysts have received wide interest due to their good electron conductivity, large specific surface area and high adsorption capacity.^{1,4,9-13} However, two dimensional (2D) graphene itself is not a semiconductor whereas 2D graphitic carbon nitride (g-C₃N₄) is.¹⁴⁻¹⁶ The polymeric g-C₃N₄ material is considered as the most stable allotrope among various carbon nitrides under ambient conditions based on its thermal stability up to 600 °C in air and perfect acid-alkali-resistance. The g-C₃N₄ is characterized in the form of 2D sheets consisting of tri-s-triazine subunits connected through planar tertiary amino groups in a layer. Importantly, g-C₃N₄ possesses a bandgap of ca. 2.7 eV, which enables it to be

a visible-light-active photocatalyst for photochemical reactions and solar energy conversion.^{17,18} Thus g-C₃N₄ has been used as a promising green metal-free photocatalyst for applications in photo-splitting water, photodecomposition of organic contaminants, and photosynthesis under visible light irradiation.¹⁴⁻²⁰ Similar to many single-component photocatalysts, g-C₃N₄ alone suffers from a high recombination rate of photoexcited charge carriers resulting in low photocatalytic performance.^{15,20,21} To break through this bottleneck, many strategies have been used improve the photocatalytic performance of g-C₃N₄ such as metal deposition,²²⁻²⁴ non-metal doping,^{25,26} fabrication of nano/mesoporous structure,^{27,28} and combination with another semiconductor.²⁹⁻³¹ Among these approaches, metal deposition demonstrates a great potential to enhance the visible light photocatalytic performance of g-C₃N₄, as the presence of metal nanoparticles is favorable for achieving efficient separation of the photogenerated charge carriers. In fact, nitrogen atoms of g-C₃N₄ play an essential role in changing the nucleation and growth behavior of deposited nanoparticles, thus resulting in great improvement of the catalytic performance. It has been reported that Ag nanoparticles (~10 nm) supported on g-C₃N₄ showed enhanced photocatalytic activity for the degradation of methyl orange (MO) under visible-light irradiation (100 mL MO solution with the initial concentration of 10 mg L⁻¹ over

100 mg catalyst).²³ Despite these progresses, it is still a challenge to further enhance the catalytic performance and improve the utilization efficiency of catalyst.

It is well known that in the semiconductor photocatalytic process, the reduction of dissolved oxygen by the conduction band electrons and the oxidation of H₂O molecules by photogenerated holes can generate superoxide (O₂^{•-}) and hydroxyl (•OH) radicals, which can rapidly and nonselectively oxidize a broad range of organic pollutants into carbon dioxide and water. Hence the degradation rate of organic pollutant can be significantly enhanced by the increasing concentration of O₂^{•-} and •OH. The DFT (density functional theory) calculation results indicate that the bottom of the conduction band (CB) of g-C₃N₄ is located at about -1.3 V (vs. NHE), which is much more negative than the standard redox potential of O₂/O₂^{•-} (-0.046 V vs. NHE), so that the CB electrons enable the reduction of dissolved O₂ molecules to generate O₂^{•-} radicals. Whereas the top of the valence band (VB) of g-C₃N₄ (~1.4 V vs. NHE) is lower than the standard redox potential of OH⁻/•OH (~1.99 V vs. NHE), thus limiting the oxidation ability of the VB holes to generate •OH radicals.^{18,23} Although hydrogen peroxide (H₂O₂) has long been used to produce •OH radicals,³² which available assist in degradation of organic molecules, relatively little attention has been paid so far to the effect of increasing O₂^{•-} radicals.

On the basis of the above-mentioned, it is therefore of great interest to use g-C₃N₄ to support much smaller sized Ag nanoparticles and introduce additional O₂^{•-} radicals for degradation reactions of organic pollutants. If that can be accomplished, then it may be feasible to achieve highly effective photocatalysis. Herein, we demonstrate a one-step facile route to fabricate g-C₃N₄ supported Ag nanoparticles (~

5.6 nm) with different Ag/g-C₃N₄ ratio. Their catalytic activities were evaluated by the degradation of methylorange (MO), methylene blue (MB), and neutral dark yellow GL (NDY-GL) under visible light irradiation. It is interesting that the degradation reactions of dyes can be accelerated significantly by adding BH₄⁻, due to the assistance of the additional O₂^{•-} radicals generated from the reduction of dissolved oxygen during the oxidation of BH₄⁻.

Results and discussion

Structure and morphology

Figure 1(a) shows XRD patterns of the pure g-C₃N₄ and Ag/g-C₃N₄ catalysts with different Ag content. The diffraction pattern of g-C₃N₄ can be assigned to the hexagonal phase of g-C₃N₄ (JCPDS 87-1526).^{24,33} There are two diffraction peaks at 2θ of 13.0° and 27.5° which can be indexed to the (100) crystal plane arising from in-planar ordering of tri-s-triazine units with a distance of 0.675 nm and (002) crystal plane of the stacking of the conjugated aromatic system with an interplanar distance of 0.326 nm, respectively. For the Ag/g-C₃N₄ catalysts, the intensity of diffraction peaks of g-C₃N₄ become weaker with increasing Ag content. However, no obvious diffraction peaks of Ag were observed for most samples due to the relatively low Ag content. Only for Ag/g-C₃N₄-8, there are two observable peaks at 2θ of 38.1° and 44.3° which can be assigned to the (111) and (200) crystal plane of the face-centered cubic structure of Ag, respectively (JCPDS 04-0783).³⁴ This result suggests the coexistence of Ag and g-C₃N₄ in the catalyst.

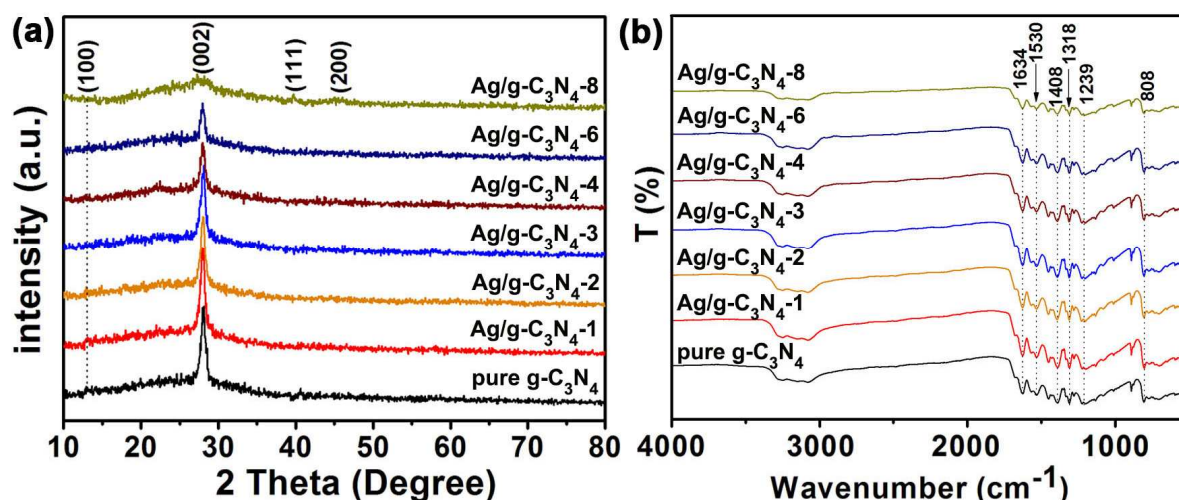


Figure 1. (a) XRD diffraction patterns and (b) FT-IR spectra of g-C₃N₄ and Ag/g-C₃N₄ catalysts with different Ag content.

The FTIR spectra of g-C₃N₄ and Ag/g-C₃N₄ catalysts with different Ag content are presented in Figure 1(b). It is obviously seen that all the absorption peaks of Ag/g-C₃N₄ catalysts with different Ag content are almost the same as those

of g-C₃N₄. The broad absorption peaks in the range of 3000-3500 cm⁻¹ are attributed to the stretching vibration of N-H and that of O-H of the physically adsorbed water, respectively. The absorption peaks at about 1634, 1530, 1408, 1318 and 1239

cm^{-1} can be ascribed to the typical stretching modes of CN heterocycles.^{33,35,36} In addition, the sharp absorption peak at 808 cm^{-1} is assigned to the characteristic breathing mode of triazine units.^{33,35,36} Figure 1S shows the Raman spectra of $\text{g-C}_3\text{N}_4$ and $\text{Ag/g-C}_3\text{N}_4$ -4, it can be clearly seen that the Raman signals of $\text{g-C}_3\text{N}_4$ in $\text{Ag/g-C}_3\text{N}_4$ -4 are greatly enhanced, which is attributed to surface-enhanced Raman scattering (SERS) effect from the supported silver nanoparticles.

The surface elemental composition and the valence states of the elements in $\text{g-C}_3\text{N}_4$ and $\text{Ag/g-C}_3\text{N}_4$ catalysts were investigated using XPS. Figure 2 shows the survey spectrum and high-resolution XPS spectra of various elements. As shown in Figure 2(a), there are C and N signals of $\text{g-C}_3\text{N}_4$ in the survey spectrum, while the peaks of C, N and Ag elements appear in the spectra of $\text{Ag/g-C}_3\text{N}_4$ -1 and $\text{Ag/g-C}_3\text{N}_4$ -4. From the high-resolution XPS spectrum of C1s shown in Figure 2(b),

the peaks centered at 284.6 eV and 288.0 eV can be ascribed to C=C and N=C=N species, respectively. Figure 2(c) presents the high-resolution XPS spectrum of N1s, which can be fitted into three components: the main peak at 398.5 eV is attributed to C-N=C coordination which originates from the sp^2 -bonded N in triazine rings, whereas the other two weak peaks at higher binding energies (around 399.6 and 401.1 eV) can be assigned to N-(C)₃ and C-N-H species, respectively.^{37,38} As shown Figure 2(d), the two peaks are located at 368.1 and 374.1 eV, corresponding to metallic Ag3d5/2 and 3d3/2 binding energy, respectively.^{39,40} Based on the results of ICP-AES analysis, the weight percentages of Ag in $\text{Ag/g-C}_3\text{N}_4$ -1, $\text{Ag/g-C}_3\text{N}_4$ -2, $\text{Ag/g-C}_3\text{N}_4$ -3, $\text{Ag/g-C}_3\text{N}_4$ -4, $\text{Ag/g-C}_3\text{N}_4$ -6 and $\text{Ag/g-C}_3\text{N}_4$ -8 were measured to be 0.73, 1.41, 1.98, 2.43, 3.95, and 4.62 wt%, respectively.

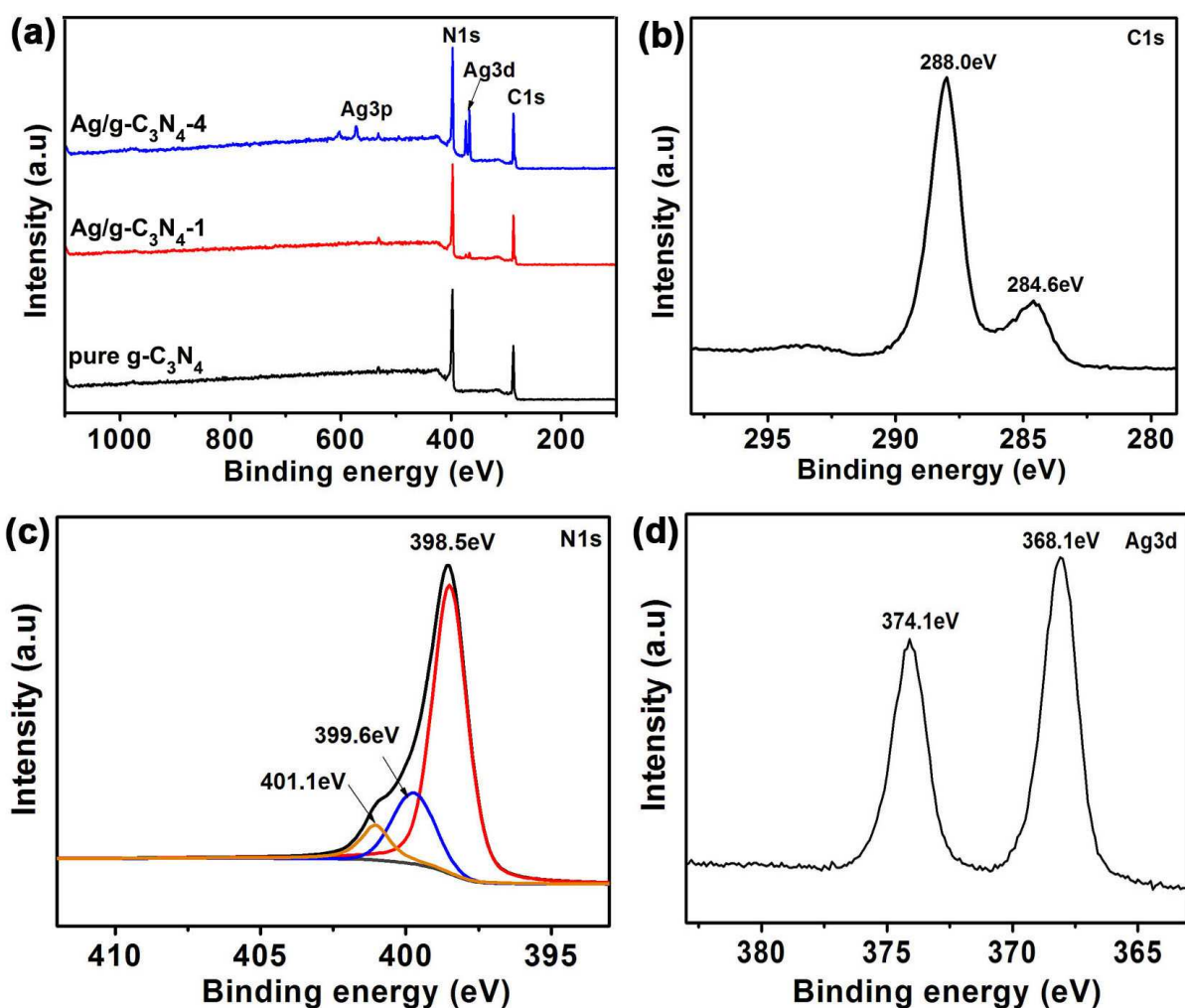


Figure 2. XPS survey spectra of $\text{g-C}_3\text{N}_4$, $\text{Ag/g-C}_3\text{N}_4$ -1 and $\text{Ag/g-C}_3\text{N}_4$ -4 (a); High resolution C1s (b) and N1s (c) and Ag3d (d) spectra of $\text{Ag/g-C}_3\text{N}_4$ -4.

TEM and FE-SEM were used to characterize the morphology and size distribution of the Ag nanoparticles on the $\text{g-C}_3\text{N}_4$ sheets. It can be clearly seen from Figure 2S that $\text{g-C}_3\text{N}_4$ has a

porous framework comprising a two-dimensional layered structure. While for the $\text{Ag/g-C}_3\text{N}_4$ -4 catalyst, the $\text{g-C}_3\text{N}_4$ sheets are decorated with highly dispersed Ag nanoparticles having an

average diameter of 5.6 nm with a narrow particle size distribution (Figure 3(a) and 3(b)). As shown in the inset of Figure 3(a), the lattice spacing of $d=0.23$ nm can be ascribed to

the (111) planes of the face-centered cubic structure of the Ag nanoparticle, which is consistent with the XRD results.

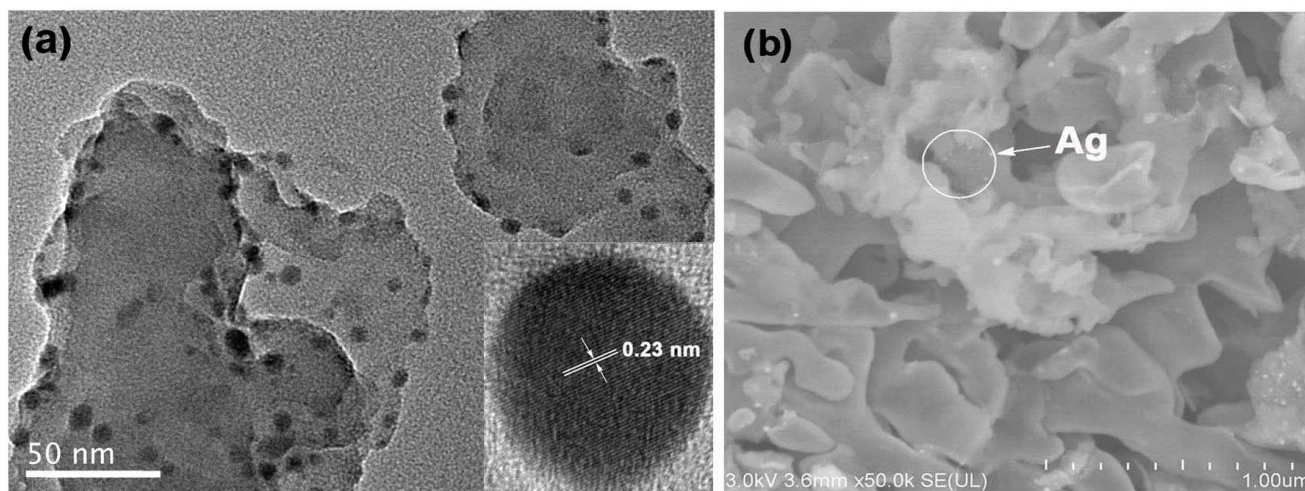


Figure 3. TEM image (a) and (b) FESEM image of Ag/g-C₃N₄-4 catalyst. The inset is the high-resolution TEM image of an Ag nanoparticle anchored on the g-C₃N₄ sheet.

Photocatalytic activity of the catalysts under visible light irradiation

The photocatalytic activities of the g-C₃N₄ and Ag/g-C₃N₄ catalysts were evaluated by the degradation of MO, MB and NDY-GL under visible light irradiation. Before the photocatalytic reaction test, the batch mode adsorption studies for the dyes were carried out by agitating catalyst (10 mg) in dye solution (10 mg L⁻¹, 50 mL) in the dark at 25 °C. As shown in Figure 3S, it is obvious that the remaining dye concentrations were still relatively high after reaching the adsorption-desorption equilibrium due to the low catalyst dosage.

Figure 4(a), (d) and (g) show the absorbance versus wavelength plots at various times for the photodegradation of MO, MB and NDY-G over Ag/g-C₃N₄-4, respectively. The blank experiment result indicates that the degradation of MO, MB and NDY-GL can be neglected in the absence of catalysts (Figure 4(b), (e) and (h)). While the photocatalytic activity of anyone of the Ag/g-C₃N₄ catalysts is higher than that of g-C₃N₄ alone. Among the catalysts with different Ag content, the Ag/g-C₃N₄-4 catalyst exhibited the best photocatalytic activity (Figure 4(b), (e) and (h)): the degradation rates of MO, MB and NDY-GL over the Ag/g-C₃N₄-4 catalyst were 86, 57, and 78 % after 120 min, respectively. The reaction processes of MO, MB and NDY-GL photocatalytic degradation over g-C₃N₄ and Ag/g-C₃N₄ catalysts with different Ag content were successfully fitted with the pseudo-first-order kinetic model and the Ag/g-C₃N₄-4 catalyst exhibited the highest rate constant of 0.01425 min⁻¹, 0.00605 min⁻¹ and 0.01305 min⁻¹ for MO, MB and NDY-GL, respectively (Figure 4(c), (f) and (i) and Table 1).

A comparative survey of recent results on the photocatalytic degradation of MO over the binary Ag/g-C₃N₄ catalysts is summarized in Table 1S,^{23,40} which shows that the degradation rate of MO over our Ag/g-C₃N₄-4 catalyst can reach up to 86% under visible light irradiation for 120 min when the catalyst dosage was as

low as 10 mg in 50 mL MO solution with an initial concentration of 10 mg L⁻¹. Obviously, the smaller-sized Ag nanoparticles can enhance the catalytic performance and achieve better utilization of the catalysts.⁴¹⁻⁴²

Table 1 The rate constants of the pseudo-first-order kinetics of MO, MB and NDY-GL photocatalytic degradation over different catalysts.

| Samples | The rate constant of pseudo-first-order kinetics (k , min ⁻¹) | | |
|---------------------------------------|--|---------|---------|
| | MO | MB | NDY-GL |
| no catalyst | 0.00011 | 0.00025 | 0.00021 |
| g-C ₃ N ₄ | 0.00201 | 0.00160 | 0.00262 |
| Ag/g-C ₃ N ₄ -1 | 0.00373 | 0.00247 | 0.00467 |
| Ag/g-C ₃ N ₄ -2 | 0.00549 | 0.00316 | 0.00559 |
| Ag/g-C ₃ N ₄ -3 | 0.00864 | 0.00454 | 0.00861 |
| Ag/g-C ₃ N ₄ -4 | 0.01425 | 0.00605 | 0.01305 |
| Ag/g-C ₃ N ₄ -6 | 0.01159 | 0.00538 | 0.01015 |
| Ag/g-C ₃ N ₄ -8 | 0.01025 | 0.00481 | 0.00898 |

On the basis of the previous work and the above experimental results, a possible mechanism for the photocatalytic degradation dyes is proposed as follows: the electron-hole pairs can be quickly generated in the g-C₃N₄ upon visible-light excitation (Eq. (1)) due to the SPR effect of metallic Ag nanoparticles, followed by instant transfer of photogenerated electrons from CB of g-C₃N₄ to the Ag nanoparticles at the interface of the Ag/g-C₃N₄ catalyst (Eq. (2)), which shifts the Fermi level to more negative potential than the standard redox potential of O₂/O₂^{•-} (-0.046 V vs. NHE), thereby the dissolved oxygen can be readily reduced by

negatively charged Ag nanoparticles to produce $O_2^{\cdot-}$ radicals (Eq. (3))^{15,23,43,44}. Finally, the dye molecules can be oxidized by $O_2^{\cdot-}$ radicals.

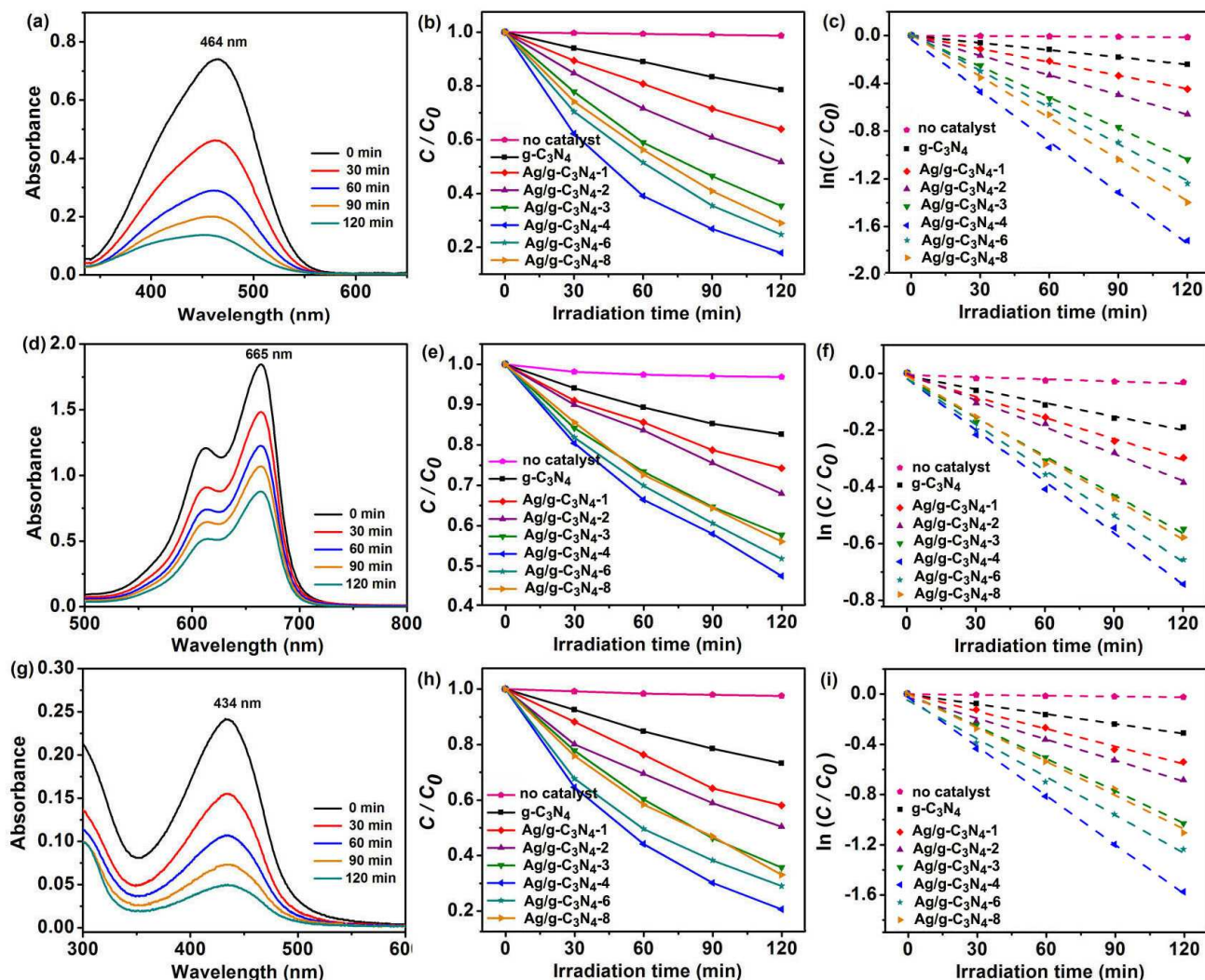
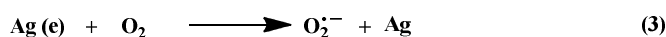
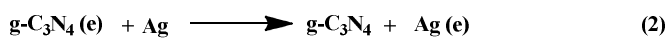
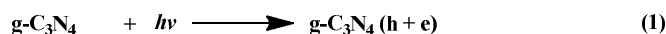


Figure 4. (a), (d) and (g) Time-dependent UV-vis absorption spectra for the degradation of MO, MB and NDY-GL over the Ag/g-C₃N₄-4 catalyst; (b), (e) and (h) Photocatalytic degradation of MO, MB and NDY-GL dyes over different catalysts; (c), (f) and (i) Plot of $\ln(c/c_0)$ against reaction time for photocatalytic degradation of MO, MB and NDY-GL with different catalysts.

Borohydride-assisted photocatalysis for dyes degradation

As shown in Figure 5(a-c), it is interesting that MO can be catalytically degraded over g-C₃N₄ and Ag/g-C₃N₄ catalysts in the presence of BH₄⁻ even in the dark at 25 °C. It should be noted that there is little change in absorbance of MO solution without catalyst before and after adding BH₄⁻ for 20 min, suggesting that the MO cannot be reduced by BH₄⁻ in aqueous solution. While the degradation rate of 15.3 % for MO over g-C₃N₄ for 20 min was observed. Furthermore, introducing a certain amount of Ag into g-C₃N₄ results in dramatical changes of catalytic activity. Among various Ag/g-C₃N₄ catalysts investigated, the Ag/g-C₃N₄-4 catalyst gave the highest MO degradation rate up to 95.5 % within 20 min in

the presence of BH₄⁻ in the dark (Figure 5(b)). In addition, catalytic degradation process of the MO over Ag/g-C₃N₄ catalysts in the presence of BH₄⁻ followed the pseudo-first-order kinetics in the dark, and the Ag/g-C₃N₄-4 catalyst exhibited the highest rate constant of 0.1589 min⁻¹ (Figure 5(c) and Table 2).

When above reactions were carried out under visible light irradiation, the degradation rate of MO over Ag/g-C₃N₄-4 catalyst reached to 98.2 % only for 8 min (Figure 5(d-e)). As shown in Figure 5(f), the degradation rates followed first-order kinetics and the Ag/g-C₃N₄-4 catalyst exhibited the highest kinetics rate constant of 0.3870 min⁻¹ (Table 2), which is 2.44 and 27.16 times that of in the presence of BH₄⁻ in the dark and in the absence of BH₄⁻ under visible light irradiation, respectively.

ARTICLE

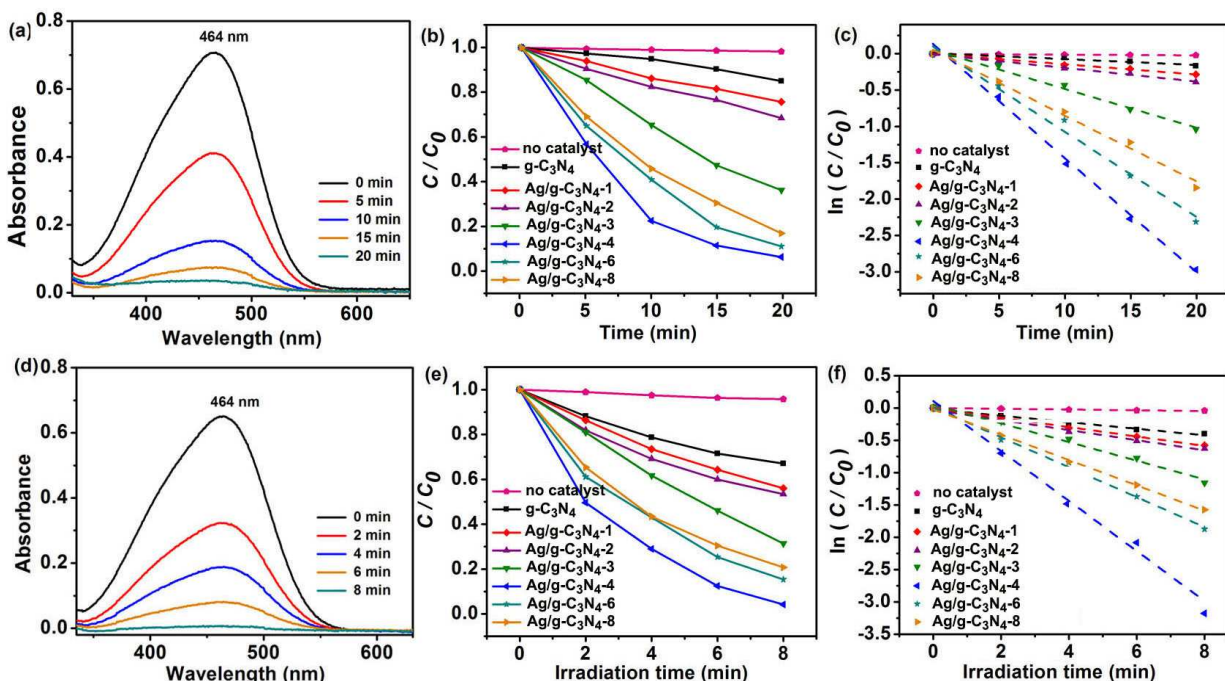


Figure 5. Time-dependent UV-vis absorption spectra for the catalytic degradation of MO over the Ag/g-C₃N₄-4 catalyst in the presence of BH₄⁻ in the dark (a) and under visible light irradiation (d); catalytic degradation of MO over different catalysts in the presence of BH₄⁻ in the dark (b) and under visible light irradiation (e); plot of ln(*c/c*₀) against reaction time for catalytic degradation of MO with different catalysts in the presence of BH₄⁻ in the dark (c) and under visible light irradiation (f).

Table 2 The rate constants of the pseudo-first-order kinetics of MO catalytic degradation over different catalysts in the presence of BH₄⁻ in the dark and under visible light irradiation.

| Samples | The rate constant of pseudo-first-order kinetics (<i>k</i> , min ⁻¹) | |
|---------------------------------------|---|---------------------------------|
| | In the dark | Under visible light irradiation |
| no catalyst | 0.00009 | 0.0057 |
| g-C ₃ N ₄ | 0.00811 | 0.0505 |
| Ag/g-C ₃ N ₄ -1 | 0.01416 | 0.0726 |
| Ag/g-C ₃ N ₄ -2 | 0.01878 | 0.0782 |
| Ag/g-C ₃ N ₄ -3 | 0.05348 | 0.1445 |
| Ag/g-C ₃ N ₄ -4 | 0.15888 | 0.3870 |
| Ag/g-C ₃ N ₄ -6 | 0.11714 | 0.2315 |
| Ag/g-C ₃ N ₄ -8 | 0.09050 | 0.1957 |

Similar results were obtained for the degradation of MB and NDY-GL in the presence of BH₄⁻ in the dark and under visible light irradiation, respectively (Figure 4-5S). It can be seen that the degradation rates of MB on Ag/g-C₃N₄-4 catalyst were 96.0 and 99.3 % in the dark for 120 min and under visible light irradiation for 45 min, respectively. The degradation rates of

NDY-GL reached to 93.8 and 99.6 % in the dark for 28 min and under visible light irradiation for 16 min, respectively.

The Ag/g-C₃N₄-4 catalyst can be used repeatedly for the degradation of dyes. Figure 6 shows that the degradation rate of MO still reached over 95 % after 6 cycles in the presence of BH₄⁻ under visible light irradiation, indicating that the catalyst is stable and effective for the degradation of organic pollutants in water.

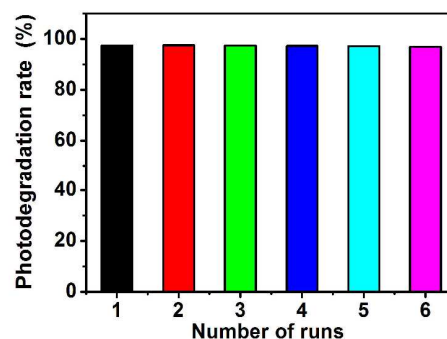


Figure 6. Bar plot showing the photodegradation rate of MO in solution for 6 cycles using Ag/g-C₃N₄-4 catalyst in the presence of BH₄⁻ under visible light irradiation.

Mechanism of borohydride-assisted photocatalysis

The above results indicate that the Ag/g-C₃N₄ catalysts not only possess the excellent visible-light-photocatalytic activity for degradation of dyes, but also have the strong ability to degrade organic molecules in the presence of BH₄⁻ even in the dark, and therefore they can exhibit the extremely superior excellent catalytic performance in the presence of BH₄⁻ under visible light irradiation. As will be seen later in this section, the high performance of the catalyst is mainly attributed to the high dispersity and smaller size of Ag nanoparticles, the synergistic effect of the combination of Ag nanoparticles and g-C₃N₄, the strong surface plasmon resonance (SPR) effect of metallic Ag nanoparticles, the efficient separation of photogenerated electron-hole pairs and the additional O₂⁻ radicals generated from the reduction of dissolved oxygen in the presence of BH₄⁻.

It is known that the optical response of hybrid metal-semiconductor system is regarded as the controlling factor for its photocatalytic activity. The optical absorption properties of g-C₃N₄ and Ag/g-C₃N₄ catalysts with different Ag content were investigated by UV-vis DRS. As shown in Figure 7(a), an obvious absorption edge of g-C₃N₄ appears at about 460 nm corresponding to the band gap of 2.7 eV, implying its visible-light-induced photocatalytic activity.^{23,45,46} While for the Ag/g-C₃N₄ catalysts, their the absorption within the visible light range (450-650 nm) is significantly extended, especially, a new absorption peak appears at around 530 nm and the intensity increases along with the Ag content. The strong and broad absorption band in the visible light region for the Ag/g-C₃N₄ catalysts can be attributed to the localized SPR effect of

metallic Ag nanoparticles, which shows efficient plasmon resonance in the visible region.^{15,47} Such an enhanced light absorption of the catalysts facilitates to yield more electron-hole pairs, which subsequently results in a higher photocatalytic activity. Moreover, the SPR effect of metallic Ag nanoparticles causes enhancement of the local electromagnetic fields, which speeds up the generation rate of photogenerated electron-hole pairs in the near-surface region of g-C₃N₄.^{43,44,48,49} The photogenerated electrons can be instantly scavenged by Ag nanoparticles at the interface of the Ag/g-C₃N₄ catalyst, creating a Schottky barrier that effectively reduces the probability of the recombination of photogenerated electron-hole pairs.^{15,43,44} This deduction is further evidenced by PL emission spectroscopy. In general, a weaker PL intensity represents a lower recombination probability of photogenerated carriers, resulting in a higher photocatalytic activity. Figure 7(b) shows the PL emission spectra of the g-C₃N₄, Ag/g-C₃N₄-4 and Ag/g-C₃N₄-4 (with BH₄⁻) under the excitation wavelength of 325 nm. The strong emission peak of g-C₃N₄ centered at 455 nm suggests a high recombination probability of photogenerated electron-hole pairs. While for Ag/g-C₃N₄-4, the significant quenching of the PL is observed in comparison with g-C₃N₄ due to the SPR effect of metallic Ag nanoparticles, indicating the strongly inhibited recombination of photoexcited carriers.^{48,49} It is worth noting that the PL intensity of Ag/g-C₃N₄-4 can be further quenched when adding BH₄⁻, this is one of reasons why adding BH₄⁻ may further enhance the catalytic activity, which will be discussed in detail later.

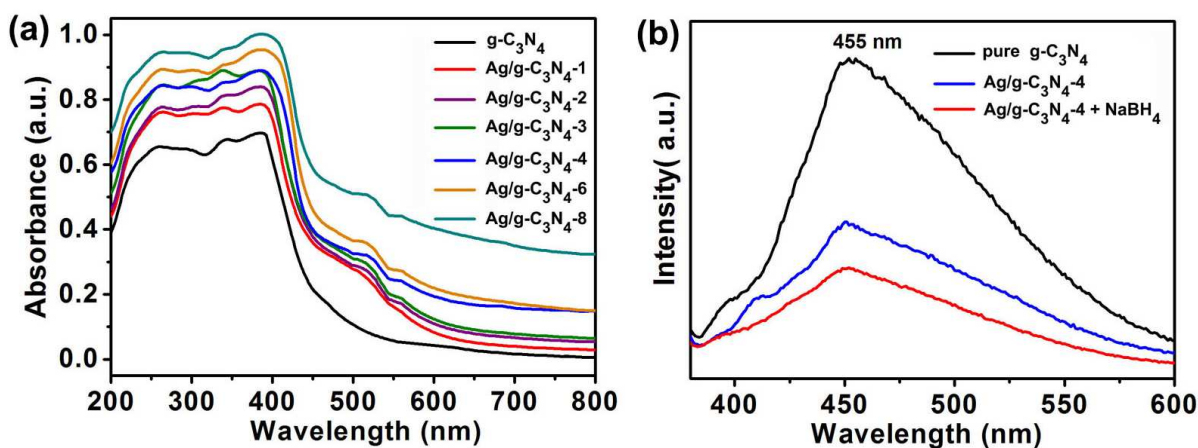


Figure 7. (a) UV-vis DRS of g-C₃N₄ and Ag/g-C₃N₄ catalysts with different Ag content; (b) Room-temperature PL emission spectra of g-C₃N₄, Ag/g-C₃N₄-4 and Ag/g-C₃N₄-4 in the presence of BH₄⁻ ($\lambda_{\text{ex}} = 325 \text{ nm}$).

The transient photocurrent response is also one of the most sensitive and powerful techniques to qualitatively estimate the separation efficiency of photogenerated carriers during the photoreactions. The transient photocurrent responses of the g-C₃N₄ and Ag/g-C₃N₄-4 electrodes were recorded for several on-off cycles of visible light irradiation in 0.5 M Na₂SO₄ aqueous solution. As shown in Figure 8, a fast and stable photocurrent response with entire reversibility is observed for each switch-on

and switch-off on both electrodes. The photocurrent response of the Ag/g-C₃N₄-4 electrode (0.25 μA) is about 5 times as high as that of g-C₃N₄ electrode (0.05 μA) due to the synergistic effect between Ag nanoparticles and g-C₃N₄. Another interesting phenomenon is that adding BH₄⁻ to the above electrolyte may further enhance the transient photocurrent responses of g-C₃N₄ and Ag/g-C₃N₄-4 electrodes. The photocurrent responses of g-C₃N₄ (0.75 μA) and Ag/g-C₃N₄-4 (0.98 μA) with BH₄⁻ (150 μL

of 0.1 g mL⁻¹ NaBH₄ aqueous solution with 0.5 M NaOH) are much higher than that of g-C₃N₄ (0.05 μA) and Ag/g-C₃N₄-4 (0.25 μA) without BH₄⁻ measured in 0.5 M Na₂SO₄ aqueous solution, respectively.

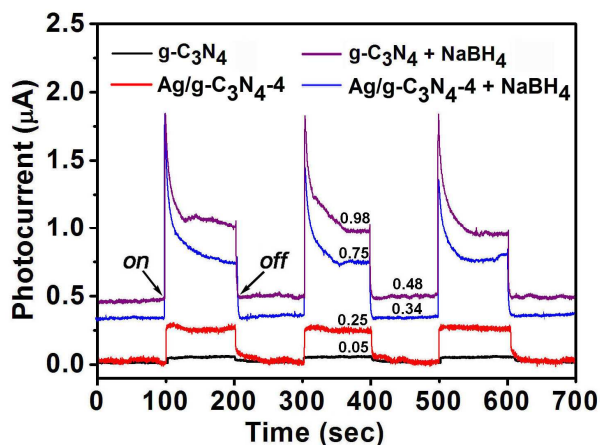
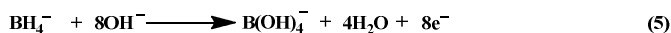


Figure 8. Photocurrent transient responses of g-C₃N₄ and Ag/g-C₃N₄-4 electrodes in 0.5 M Na₂SO₄ aqueous solution with BH₄⁻ and without BH₄⁻.

It has been reported that the oxidation reaction of BH₄⁻ on electrode materials (such as Au, Ag, Pt, Pd, etc) is in parallel with its hydrolysis proceeds, which can be described as the following equation⁵⁰⁻⁵³:

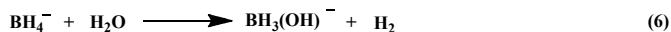


Because both the bottom of the CB of g-C₃N₄ and the aligned Fermi energy level of Ag are located at more negative values than the standard redox potential of complete eight-electron oxidation process (-1.24 V vs. SHE), it is entirely possible that the complete oxidation of BH₄⁻ becomes the predominant reaction^{51,53}:

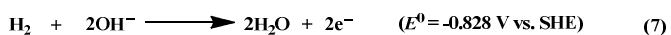


On the basis of above analyses, we can conclude that the BH₄⁻ ions in aqueous alkaline medium can be directly oxidized on the surface of g-C₃N₄ or Ag/g-C₃N₄-4 and the released electrons are quickly transferred to the ITO electrode, resulting in the current responses.

It is found that even in the dark, g-C₃N₄ and Ag/g-C₃N₄-4 with BH₄⁻ also exhibited considerable current responses of 0.34 μA and 0.48 μA, respectively. In this case, the hydrolysis reaction of BH₄⁻ may be represented as:



The resulting H₂ on the electrode surface can also be oxidized by hydroxyl ions with the release of two electrons:⁵⁰



As a result, the chemically generated electrons can be instantly transferred to the ITO electrode, leading to the current responses.

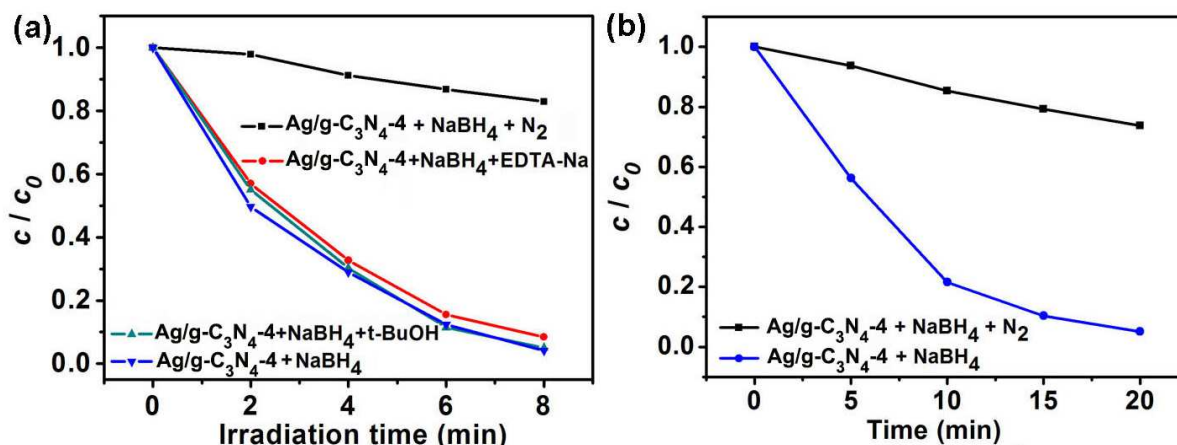


Figure 9 Influence of various trapping agents on the MO catalytic degradation in the presence of Ag/g-C₃N₄-4 catalyst and BH₄⁻ under visible-light irradiation (a) and in the dark (b).

As widely accepted, the active species (such as •OH, O₂⁻ and the photogenerated holes) play important roles in degrading organic pollutants. For better understanding the photocatalytic mechanism of the MO degradation over Ag/g-C₃N₄ in the presence of BH₄⁻, the active species were measured through trapping by tert-butyl alcohol (t-BuOH, 1 mmol L⁻¹) as a hydroxyl radical scavenger and disodium ethylenediamine tetraacetate dehydrate (EDTA-2Na, 1 mmol L⁻¹) as a hole scavenger, respectively.⁵⁴ As can be seen Figure 9(a), the change of the photodegradation rate of MO was unnoticeable when adding t-BuOH, suggesting that there were few •OH radicals in the photocatalytic system. This may be ascribed to

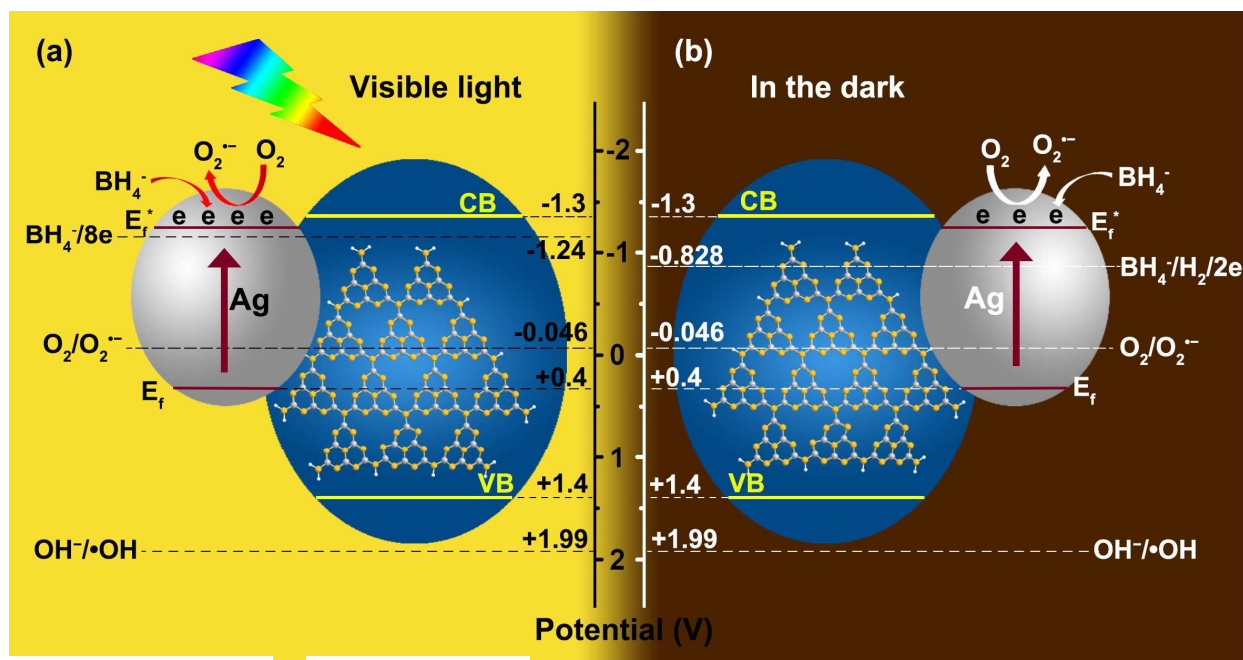
that the top of the valence band (VB) of g-C₃N₄ is lower than the standard redox potential of OH⁻/•OH, and therefore the photogenerated holes on VB cannot oxidize OH⁻ to give •OH radicals (Scheme 1).²³ Similarly, the change of the photodegradation rate of MO was not obvious when adding EDTA-2Na, implying that the photogenerated holes were not the main active species in the photocatalytic process. However, whether under visible light irradiation or in the dark, the photodegradation of MO in the presence of BH₄⁻ was greatly reduced when the reaction system was purged with pure N₂ to remove dissolved O₂ (Figure 9(a) and (b)). Accordingly, we can conclude that O₂⁻ radicals are the main active species for the

catalytic degradation process of MO over Ag/g-C₃N₄-4 in the presence of BH₄⁻ under visible light irradiation or in the dark.⁵⁵ The generation of O₂⁻ radicals in the catalytic process was confirmed by a color reaction between the ferrous ions (Fe²⁺) and nitric oxide (NO), resulting in a brown [FeNO]²⁺ complex, as shown in Figure 6S.

On the basis of the above result of active species trapping experiments, the O₂⁻ radicals as the main active species play a key role in the catalytic degradation process of MO over Ag/g-C₃N₄-4 in the presence of BH₄⁻ under visible light irradiation or in the dark, while the role of photogenerated holes could be negligible. A possible generation mechanism of the O₂⁻ radicals is proposed as in Scheme 1(a): both the bottom of the CB of g-C₃N₄ and the aligned Fermi energy level of Ag are located at more negative values than the standard redox potential of complete eight-electron oxidation process (-1.24 V vs. SHE). Therefore, the BH₄⁻ can be oxidized directly on the aligned Fermi energy level of Ag under visible light irradiation in aqueous alkaline medium to release 8 electrons (Eq. (5)), which can attack the adsorbed oxygen to produce O₂⁻ radicals

(Eq. (3)). Consequently, the resulting O₂⁻ radicals helped to significantly speed up the degradation when adding BH₄⁻ and the photocatalytic degradation rates of MO, MB and NDY-GL reached up to 98.2, 99.3 and 99.6% only for 8, 45, and 16 min visible light irradiation, respectively (Figure 5, Figure 4S and Figure 5S).

As mentioned before, the degradation rates of MO, MB and NDY-GL over Ag/g-C₃N₄-4 reached up to 95.5, 96.0 and 93.8% for 20, 120, 28 min, respectively, in the presence of BH₄⁻ in the dark. Based on the results of catalytic degradation experiments and transient photocurrent measurements in the dark (Figure 5, Figure 4S and Figure 5S), a possible mechanism for the catalytic activity enhancement in the dark is proposed as shown in Scheme 1(b). The excellent catalytic activity may be contributed to the fact that, as the hydrolysis product of the BH₄⁻ (Eq. (6)), H₂ can be oxidized to H₂O with the release of 2 electrons (Eq. (7)) on the surface of Ag/g-C₃N₄ and the resulting electrons may transfer to the adsorbed oxygen to generate O₂⁻ radicals.



Scheme 1 Proposed mechanism of the O₂⁻ radicals generation.

Conclusions

In summary, a visible-light-driven Ag/g-C₃N₄ catalyst with different Ag content has been successfully prepared via a facile one-step route. Morphology observation indicates that g-C₃N₄ sheets were evenly decorated with Ag nanoparticles having an average diameter of 5.6 nm and narrow particle size distribution. The photocatalytic activity measurements demonstrate that the photocatalytic degradation rates of MO, MB and NDY-GL over Ag/g-C₃N₄-4 reached up to 98.2, 99.3 and 99.6% in the presence of BH₄⁻ only for 8, 45, and 16 min visible light irradiation, respectively. The significant enhancement in photoactivity of the catalyst can be ascribed to

the high dispersity and smaller size of Ag nanoparticles, the strong surface plasmon resonance (SPR) effect of metallic Ag nanoparticles, the efficient separation of photogenerated electron-hole pairs, the additional O₂⁻ radicals generated by the reduction of dissolved oxygen in the presence of BH₄⁻ and the synergistic effect of Ag nanoparticles and g-C₃N₄.

Experimental

Preparation of g-C₃N₄ Nanosheets

All chemicals and reagents used in this study were of analytical grade and were used without further purification. The bulk g-C₃N₄ was synthesized according to a procedure reported

previously²³: 5 g of dicyandiamide was added into a crucible covered loosely with a lid and heated at 2 °C/min up to 530 °C in a muffle furnace for 4 h. After the reaction, the yellow bulk g-C₃N₄ was obtained. The g-C₃N₄ nanosheets were prepared by exfoliating the as-prepared bulk g-C₃N₄ in the ultrapure water. In brief, 50 mg of g-C₃N₄ was dispersed into 100 mL of ultrapure water with sonication for 24 h. The resulting suspension was centrifuged at 3000 rpm to remove the residual unexfoliated g-C₃N₄, followed by centrifugation at 15000 rpm to obtain g-C₃N₄ nanosheets.

Preparation of Ag/g-C₃N₄ Catalysts

Ag/g-C₃N₄ catalysts with different Ag content (1, 2, 3, 4, 5, 6, 8 wt %) were synthesized. Typically, the procedure for the synthesis of Ag/g-C₃N₄ catalyst with 1% Ag content is as follows: 99 mg of the as-obtained g-C₃N₄ nanosheets was added into 50 mL of ultrapure water with sonication for 1 h. Then 20 μL of AgNO₃ (1 mg of Ag content) aqueous solution was added to above g-C₃N₄ nanosheets dispersion. The mixture was stirred for 30 min at room temperature, followed by adding the freshly prepared NaBH₄ aqueous solution (20 μL, 0.3 g mL⁻¹). The reaction mixture was continuously stirred for 60 min at room temperature. After that, the mixture was centrifuged at 10000 rpm, and the product was washed and dried through freeze drying and labeled as Ag/g-C₃N₄-1.

Characterization

The crystallinity and phase of Ag/g-C₃N₄ catalysts were characterized by X-ray diffraction (XRD) on a Bruker D8 Advanced diffractometer with Cu K α radiation (λ =1.5418 Å) and the scanning angle ranged from 10° to 80° of 2 θ . The chemical composition of the samples was analyzed by X-ray photoelectron spectroscopy (XPS) on a RBD upgraded PHI-5000C ESCA system (Perkin Elmer) with Mg K radiation ($h\nu$ =1253.6 eV). The peak positions were internally referenced to the C 1s peak at 284.6 eV. The Ag content in the Ag/g-C₃N₄ catalysts was determined by inductively coupled plasma atomic emission spectrometry (ICP-AES, Shimadzu ICP-7510). The morphologies and structure were examined with transmission electron microscopy (TEM; JEOL JEM-2100) and field-emission scanning electron microscopy (FESEM; LEO1550). Fourier transform-infrared (FT-IR) spectra were recorded on a Bruker VECTOR 22 spectrometer using the KBr pellet technique. Raman spectra were acquired on a Renishaw inVia Reflex Raman Microprobe. Ultraviolet-visible (UV-vis) diffuse reflection spectra (DRS) were carried out on a Shimadzu UV-3100 spectrophotometer in the wavelength range of 200-800 nm with BaSO₄ as reference. Photoluminescence (PL) spectra were recorded on a Jobin Yvon SPEX Fluorolog-3-P spectroscopy and a 450 W Xe lamp was used as the excitation source with excitation wavelength of 325 nm. Photocurrent measurements were carried out on a CHI 660D electrochemical workstation in a standard three-electrode system using the prepared samples as the working electrodes with an active area of ca. 0.5 cm². Platinum foil and a saturated calomel electrode (SCE) were used as the counter and reference electrodes,

respectively. Photocurrent measurements were performed in 1 M Na₂SO₄ by using 500W xenon lamp with a 420 nm cutoff filter (the average light intensity was 31.2 mWcm⁻²) as the source of visible light irradiation.

Catalytic activity measurement

The photocatalytic activity of the as-prepared catalysts was evaluated by the degradation of methyorange (MO), methylene blue (MB), and neutral dark yellow GL (NDY-GL) under visible light irradiation. Photo-irradiation was carried out using a 500 W xenon lamp with UV cut-off filters (JB450) to completely remove any radiation below 420 nm and to ensure illumination by visible-light only. Experiments were conducted at ambient temperature as follows: take MO for instance, 10 mg of catalyst was added to 50 mL of a 10 mg L⁻¹ dye aqueous solution. Before starting the illumination, the reaction mixture was stirred for 60 min in the dark to reach the adsorption-desorption equilibrium between the dye and the catalyst. After adding 150 μL of 0.1 g mL⁻¹ NaBH₄ aqueous solution with 0.5 M NaOH to the above reaction mixture, the lamp was turned on. At a given time interval of irradiation, 5 mL aliquots were withdrawn, and then centrifuged to remove essentially all the catalyst. The concentrations of the remnant dye were spectrophotometrically monitored by measuring the absorbance of solutions at 464 nm during the photodegradation process.

Acknowledgements

This work was supported by NNSF of China (No. 51472120), NSAF (No. U1230125), RFDP (No. 20123219130003), China Postdoctoral Science Foundation (No. 2014M561651), Jiangsu Planned Projects for Postdoctoral Research Funds (No. 1401003B), the Fundamental Research Funds for the Central Universities (No. 20915011311, No. 30920140122003, No. 30920140122008), the Opening Project of the Jiangsu Key Laboratory for Environment Functional Materials (No. SJHG1303), the Zijin Intelligent Program of NUST (2014) and PAPD of Jiangsu.

Notes and references

¹ Key Laboratory for Soft Chemistry and Functional Materials of Ministry Education, Nanjing University of Science and Technology, 210094, Nanjing, China. Address correspondence to wangx@njjust.edu.cn (X. Wang) or zhujw@njjust.edu.cn (J. W. Zhu).

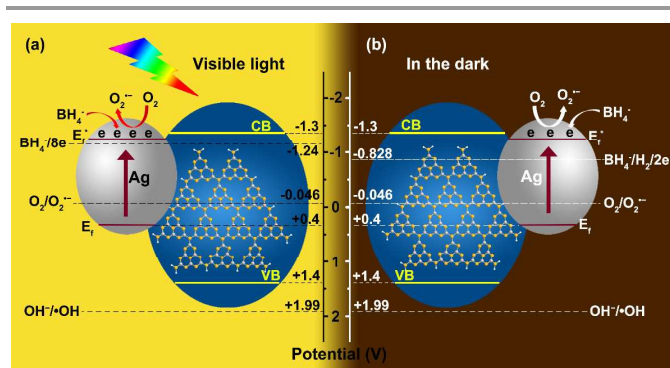
² Jiangsu Key Laboratory for Chemistry of Low-Dimensional Materials, Huaiyin Normal University, Huai'an, Jiangsu 223300, PR China. Address correspondence to zll@hytc.edu.cn (L. L. Zhang)

[†] These authors contributed equally to this work.

Electronic Supplementary Information (ESI) available: The typical experiment details for the color reaction between the ferrous ions (Fe²⁺) and nitric oxide (NO); MO photodegradation performances in the presence of Ag/g-C₃N₄ or Ag/g-C₃N₄/TiO₂ nanocomposites; TEM image of pure g-C₃N₄ catalyst; The remaining MO, MB and NDY-GL in solution after reaching the adsorption-desorption equilibrium in the dark for 60 min with stirring; Catalytic degradation of MB and NDY-GL over Ag/g-C₃N₄-4 catalyst in the presence of BH₄⁻ in the dark and under visible light irradiation. See DOI: 10.1039/b000000x/

- 1 Q. Xiang, J. Yu and M. Jaroniec, *Chem. Soc. Rev.*, 2012, **41**, 782-796.
- 2 D. Wang and D. Astruc, *Chem. Rev.*, 2014, **114**, 6949-6985.
- 3 C. Huang, C. Li and G. Shi, *Energy Environ. Sci.*, 2012, **5**, 8848-8868.
- 4 W. Tu, Y. Zhou and Z. Zou, *Adv. Funct. Mater.*, 2013, **23**, 4996-5008.
- 5 L. Q. Liu, T. D. Dao, R. Kodiyath, Q. Kang, H. Abe, T. Nagao and J. H. Ye, *Adv. Funct. Mater.*, 2014, **24**, 7754-7762.
- 6 G. Zhang, G. Kima and W. Choi, *Energy Environ. Sci.*, 2014, **7**, 954-966.
- 7 B. Weng, S. Q. Liu, N. Zhang, Z. R. Tang and Y. J. Xu, *J. Catal.*, 2014, **309**, 146-155.
- 8 M. Zhang, J. Xu, R. L. Zong and Y. F. Zhu, *Appl. Catal. B: Environ.*, 2014, **147**, 229-235.
- 9 F. K. Meng, S. K. Cushing, J. T. Li, S. M. Hao and N. Q. Wu, *ACS Catal.*, 2015, **5**, 1949-1955.
- 10 W. Y. Gao, M. Q. Wang, C. X. Ran, X. Yao, H. H. Yang, J. Liu, D. L. He, J. B. Bai, *Nanoscale*, 2014, **6**, 5498-5508.
- 11 Y. H. Ng, S. Ikeda, M. Matsumura, R. Amal, *Energy Environ. Sci.*, 2012, **5**, 9307-9318.
- 12 Q. Li, X. Li, S. Wageh, A. A. Al-Ghamdi and J. Yu, *Adv. Energy Mater.*, 2015, DOI: 10.1002/aenm.201500010.
- 13 M. Yang, N. Zhang, M. Pagliaro and Y. Xu, *Chem. Soc. Rev.*, 2014, **43**, 8240-8254.
- 14 G. Algara-Siller, N. Severin, S. Y. Chong and T. Björkman, *Angew. Chem.*, 2014, **126**, 7580-7585.
- 15 Z. W. Zhao, Y. J. Sun and F. Dong, *Nanoscale*, 2015, **7**, 15-37.
- 16 J. Zhuang, W. Lai, M. Xu, Q. Zhou and D. Tang, *ACS Appl. Mater. Interfaces*, 2015, **7**, 8330-8338.
- 17 X. Wang, K. Maeda, A. Thomas, K. Takanebe, G. Xin, J. M. Carlsson, K. Domen and M. Antonietti, *Nat. Mater.*, 2009, **8**, 76-80.
- 18 X. Wang, S. Blechert and M. Antonietti, *ACS Catal.*, 2012, **2**, 1596-1606.
- 19 Y. Wang, X. C. Wang and M. Antonietti, *Angew. Chem., Int. Ed.*, 2012, **51**, 68-89.
- 20 S. Cao, J. Low, J. Yu and M. Jaroniec, *Adv. Mater.*, 2015, DOI: 10.1002/adma.201500033.
- 21 G. Dong, Y. Zhang, Q. Pan and J. Qiu, *J. Photochem. Photobiol. C*, 2014, **20**, 33-50.
- 22 K. Tian, W. Liu and H. Jiang, *ACS Sustainable Chem. Eng.*, 2014, DOI: 10.1021/sc500646.
- 23 Y. Yang, Y. Guo, F. Liu, X. Yuan, Y. Guo, S. Zhang, W. Guo and M. Huo, *Appl. Catal. B*, 2013, **142-143**, 828-837.
- 24 N. Cheng, J. Tian, Q. Liu, C. Ge, A. H. Qusti, A. M. Asiri, A. O. Al-Youbi and X. Sun, *ACS Appl. Mater. Interfaces*, 2013, **5**, 6815-6819.
- 25 G. Liu, P. Niu, C. Sun, S. C. Smith, Z. Chen, G. Q. Lu and H. M. Cheng, *J. Am. Chem. Soc.*, 2010, **132**, 11642-11648.
- 26 Y. J. Zhang, T. Mori, J. H. Ye and M. Antonietti, *J. Am. Chem. Soc.*, 2010, **132**, 6294-6295.
- 27 F. Z. Su, S. C. Mathew, G. Lipner, X. Z. Fu and M. Antonietti, *J. Am. Chem. Soc.*, 2010, **132**, 16299-16301.
- 28 K. Kailasam, J. D. Epping, A. Thomas, S. Losse and H. Junge, *Energy Environ. Sci.*, 2011, **4**, 4668-4674.
- 29 Y. Wang, R. Shi, J. Lin and Y. Zhu, *Energy Environ. Sci.*, 2011, **4**, 2922-2929.
- 30 Y. He, J. Cai, T. Li, Y. Wu, Y. Yi, M. Luo and L. Zhao, *Ind. Eng. Chem. Res.*, 2012, **51**, 14729-14737.
- 31 H. Katsumata, T. Sakai, T. Suzuki and S. Kaneco, *Ind. Eng. Chem. Res.*, 2014, **53**, 8018-8025.
- 32 Y. Fu, X. Wang, *Ind. Eng. Chem. Res.*, 2011, **50**, 7210-7218.
- 33 Y. Fu, J. Zhu, C. Hu, X. Wu and X. Wang, *Nanoscale*, 2014, **6**, 12555-12564.
- 34 Y. Ding, Y. Wang, L. Su, H. Zhang and Y. Lei, *J. Mater. Chem.*, 2010, **20**, 9918-9926.
- 35 Q. Xiang, J. Yu and M. Jaroniec, *J. Phys. Chem. C*, 2011, **115**, 7355-7363.
- 36 W. Wang, J. C. Yu, D. Xia, P. K. Wong and Y. Li, *Environ. Sci. Technol.*, 2013, **47**, 8724-8732.
- 37 Y. Li, H. Zhang, P. Liu, D. Wang, Y. Li and H. Zhao, *Small*, 2013, **9**, 3336-3344.
- 38 L. Y. Feng, L. Q. Yang, Z. J. Huang, J. Y. Luo, M. Li, D. B. Wang and Y. G. Chen, *Sci. Rep.*, 2013, doi:10.1038/srep03306.
- 39 L. Ge, M. X. Xu and H. B. Fang, *J. Mol. Catal. A Chem.*, 2006, **256**, 68-76.
- 40 L. Ge, C. Han, J. Liu and Y. Li, *Appl. Catal. A: Gen.*, 2011, **409-410**, 215-222.
- 41 Y. Chen, W. Huang, D. He, Y. Situ and H. Huang, *ACS Appl. Mater. Interfaces*, 2014, **6**, 14405-14414.
- 42 S. Zhang, J. Li, X. Wang, Y. Huang, M. Zeng and J. Xu, *ACS Appl. Mater. Interfaces*, 2014, **6**, 22116-22125.
- 43 D. B. Ingram, P. Christopher, J. L. Bauer and S. Linic, *ACS Catal.*, 2011, **1**, 1441-1447.
- 44 C. Wen, A. Yin and W. Dai, *Appl. Catal. B: Environ.*, 2014, 160-161, 730-741.
- 45 X. Bai, R. Zong, C. Li, D. Liu, Y. Liu and Y. Zhu, *Appl. Catal. B: Environ.*, 2014, **147**, 82-91.
- 46 M. Xu, L. Han and S. Dong, *ACS Appl. Mater. Interfaces*, 2013, **5**, 12533-12540.
- 47 X. Li, J. Yu, J. Low, Y. Fang, J. Xiao and X. Chen, *J. Mater. Chem. A*, 2015, **3**, 2485-2534.
- 48 W. Hou and S. B. Cronin, *Adv. Funct. Mater.*, 2013, **23**, 1612-1619.
- 49 S. Linic, P. Christopher and D. B. Ingram, *Nature Mater.*, 2011, **10**, 911-921.
- 50 J. Ma, N. A. Choudhury and Y. Saha, *Renew. Sust. Energ. Rev.*, 2010, **14**, 183-199.
- 51 D. Duan, S. Liu, Y. Sun, *J. Power Sources*, 2012, **210**, 198-203.
- 52 H. Qin, L. Jiang, Y. He, J. Liu, K. Cao, J. Wang and Z. Ji, *J. Mater. Chem. A*, 2013, **1**, 15323-15328.
- 53 B. Šljukić, J. Milikić, D. M. Santos, C. A. Sequeira, D. Maccio and A. Saccone, *J. Power Sources*, 2014, **272**, 335-343.
- 54 Y. Fu, H. Chen, X. Sun, X. Wang, *Appl. Catal. B: Environ.*, 2012, 111-112, 280-287.
- 55 C. Pan and Y. Zhu, *Environ. Sci. Technol.*, 2010, **44**, 5570-5574.

Table of contents graphic



The Ag/g-C₃N₄ catalyst exhibits superior catalytic performance for the degradation of dyes by the assistance of the additional O₂⁻ radicals generated from the reduction of dissolved oxygen during the oxidation of BH₄⁻.